Monthly Notices
of the
ROYAL ASTRONOMICAL SOCIETY

MNRAS **476,** 459–469 (2018) doi:10.1093/mnras/sty223

Methods for multiple-telescope beam imaging and guiding in the near-infrared

N. Anugu,[1,2,3★] A. Amorim,[4,5★] P. Gordo,[4,5] F. Eisenhauer,[6] O. Pfuhl,[6] M. Haug,[6] E. Wieprecht,[6] E. Wiezorrek,[6] J. Lima,[4,5] G. Perrin,[7] W. Brandner,[8] C. Straubmeier,[9] J.-B. Le Bouquin[10] and P. J. V Garcia[1,2★]

[1]*Faculdade de Engenharia, Universidade do Porto, rua Dr Roberto Frias, P-4200-465 Porto, Portugal*
[2]*CENTRA – Centro de Astrofísica e Gravitação, IST, Universidade de Lisboa, P-1049-001 Lisboa, Portugal*
[3]*School of Physics, Astrophysics Group, University of Exeter, Stocker Road, Exeter EX4 4QL, UK*
[4]*Universidade de Lisboa – Faculdade de Ciências, Campo Grande, P-1749-016 Lisboa, Portugal*
[5]*CENTRA – Centro de Astrofísica e Gravitação, IST, Universidade de Lisboa, P-1049-001 Lisboa, Portugal*
[6]*Max Planck Institute for Extraterrestrial Physics, Giessenbachstr, D-85748 Garching, Germany*
[7]*Observatoire de Paris Meudon, F-92195 Meudon Cedex, Paris, France*
[8]*Max-Planck-Institut für Astronomie, Königstuhl 17, D-69117, Heidelberg, Germany*
[9]*1 Physikalisches Institut, Universität zu Köln, Zülpicher Str. 77, D-50937 Köln, Germany*
[10]*Institut de Planétologie et d'Astrophysique de Grenoble (IPAG), Grenoble, France*

Accepted 2018 January 23. Received 2018 January 15; in original form 2017 November 19

ABSTRACT

Atmospheric turbulence and precise measurement of the astrometric baseline vector between any two telescopes are two major challenges in implementing phase-referenced interferometric astrometry and imaging. They limit the performance of a fibre-fed interferometer by degrading the instrument sensitivity and the precision of astrometric measurements and by introducing image reconstruction errors due to inaccurate phases. A multiple-beam acquisition and guiding camera was built to meet these challenges for a recently commissioned four-beam combiner instrument, GRAVITY, at the European Southern Observatory Very Large Telescope Interferometer. For each telescope beam, it measures (a) field tip-tilts by imaging stars in the sky, (b) telescope pupil shifts by imaging pupil reference laser beacons installed on each telescope using a 2×2 lenslet and (c) higher-order aberrations using a 9×9 Shack–Hartmann. The telescope pupils are imaged to provide visual monitoring while observing. These measurements enable active field and pupil guiding by actuating a train of tip-tilt mirrors placed in the pupil and field planes, respectively. The Shack–Hartmann measured quasi-static aberrations are used to focus the auxiliary telescopes and allow the possibility of correcting the non-common path errors between the adaptive optics systems of the unit telescopes and GRAVITY. The guiding stabilizes the light injection into single-mode fibres, increasing sensitivity and reducing the astrometric and image reconstruction errors. The beam guiding enables us to achieve an astrometric error of less than 50 μas. Here, we report on the data reduction methods and laboratory tests of the multiple-beam acquisition and guiding camera and its performance on-sky.

Key words: atmospheric effects – instrumentation: adaptive optics – instrumentation: high angular resolution – instrumentation: interferometers.

1 INTRODUCTION

GRAVITY (GRAVITY Collaboration et al. 2017a) is a dual feed phase referencing interferometric imaging and a narrow-angle astrometric instrument. It was built for the European Southern Observatory (ESO) Very Large Telescope Interferometer (VLTI) to monitor stellar sources in the vicinity of the supermassive black hole at the Galactic Centre (Genzel, Eisenhauer & Gillessen 2010; Eisenhauer et al. 2011). It combines four beams coherently in the *K* band of either the unit telescopes (UTs, 8 m) or the auxiliary telescopes (ATs, 1.8 m). It is designed to deliver a differential astrometry of around 10 μas and an angular resolution of around 4 mas. It

★ E-mail: n.anugu@exeter.ac.uk (NA); antonio.amorim@sim.fc.ul.pt (AA); pgarcia@fe.up.pt (PJVG)

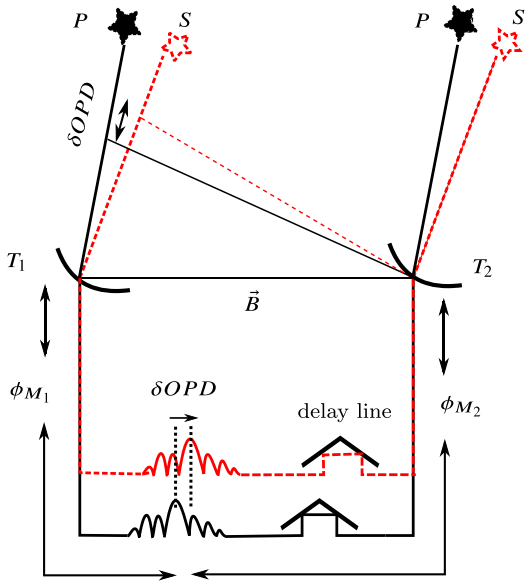

Figure 1. GRAVITY working principle. The beams for the science S and reference P stars are combined simultaneously. The GRAVITY metrology system measures the differential optical path between the two stars introduced by the VLTI beam relay and the GRAVITY beam-combiner instrument. ϕ_{M_1} and ϕ_{M_2} are the phases between the beam combiner and the telescopes (T_1 and T_2). $\boldsymbol{B}$ is the baseline vector.

works by observing a reference star at position $\boldsymbol{P}$ and a science star at position $\boldsymbol{S}$. Fringes for each star are obtained in separate beam combiners (Fig. 1). The differential separation of stars in the sky is proportional to the differential optical path difference (δOPD) observed in the beam-combiner instrument. For a first-order approximation, the differential optical path difference is related to the differential separation of the stars and the baseline vector ($\boldsymbol{B}$) by

$$\delta\mathrm{OPD} = (\boldsymbol{S} - \boldsymbol{P}) \cdot \boldsymbol{B}.$$

The coherent beam combination of the stars' light is implemented using a single-mode fibre-fed integrated optics chip (Benisty et al. 2009; Jocou et al. 2014). The δOPD between the science and reference beam combiners is measured with a dedicated laser metrology system (Lippa et al. 2016; GRAVITY Collaboration et al. 2017a).

Adaptive optics correction residuals such as slow field drifts (tip/tilts) and non-common path aberrations and telescope/optical pupil motions[1] (lateral and longitudinal or pupil defocus shifts) need to be corrected. They degrade the performance in terms of (a) instrument sensitivity, because of starlight injection problems into the single-mode fibres in the presence of field drifts, (b) astrometric errors due to field drifts and pupil shifts causing a baseline paradox (Colavita 2009; Woillez & Lacour 2013; Lacour et al. 2014) and (c) image reconstruction errors due to inaccurate phases.[2]

The astrometric error caused by field tip-tilts ($\Delta\alpha$) and lateral (ΔL_x) and longitudinal (ΔL_z) pupil shifts (Fig. 2, Lacour et al. 2014) is

$$\sigma_\mathrm{T} \sim \frac{\Delta L_\mathrm{x} \sin(\Delta\alpha) + \Delta L_\mathrm{z}\left[1 - \cos(\Delta\alpha)\right]}{B} \quad [\mathrm{rad}]. \qquad (1)$$

[1] Optical train vibrations cause pupil motion while tracking the object of interest with the delay lines.

[2] Of relevance for, e.g., imaging stellar high signal-to-noise surfaces.

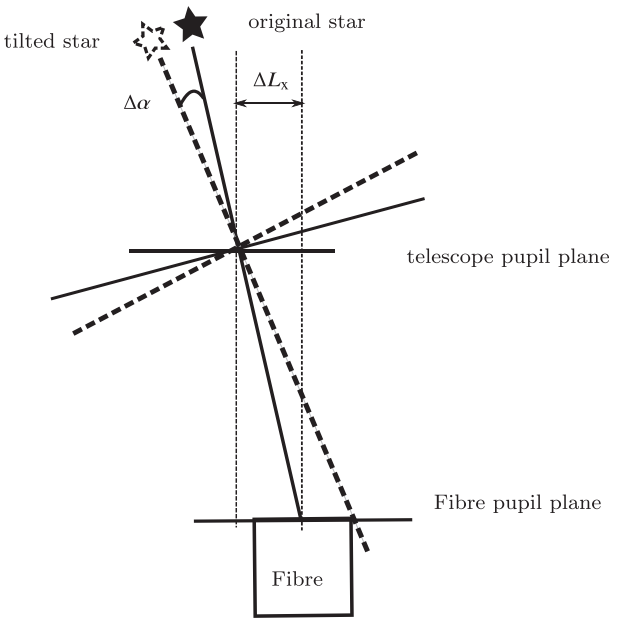

Figure 2. Influence of field drift and pupil lateral shift in the beam while injecting light into a single-mode fibre. The star shown as a dashed line is tilted ($\Delta\alpha$) with respect to the original star (solid line). The telescope pupil is shifted laterally (ΔL_x) with respect to the fibre pupil.

To achieve the GRAVITY goal of 10 μas astrometric precision, the telescope beams must be corrected with residuals in the field to less than 10 mas root-mean-square (rms) deviation error,[3] the lateral pupil to less than 40 mm rms and the longitudinal pupil to less than 10 km rms at the UTs (Lacour et al. 2014). To enable these corrections, a four-beam imaging and guiding instrument, the multiple-beam acquisition and guiding camera, was built.

This paper is presented as follows. In Section 2, the optical layout and functions of the multiple-beam acquisition and guiding camera are briefly described. The extraction of the beam guiding parameters from the image are presented in Section 3. Sections 4 and 5 present the validation of the instrument concepts and the characterization results at the laboratory and on-sky. The paper ends with a summary and conclusions.

2 OPTICAL FUNCTIONS OF THE MULTIPLE-BEAM ACQUISITION AND GUIDING CAMERA

2.1 Overall optical layout

The multiple-beam acquisition and guiding camera is a subsystem of GRAVITY. It has two sub-units: (a) the external folding optics and (b) the core beam analyser. The folding optics sub-unit has four optical entrance channels, accepts four 18 mm near-infrared beams and redirects them into the beam analyser. The beam analyser is the core of the multiple-beam acquisition and guiding camera. It implements four important optical functions (Fig. 3): (a) the pupil tracker measures the telescope pupil shifts, (b) the aberration sensor measures quasi-static wavefront aberrations, (c) the pupil imager images the telescope pupil and (d) the field imager images the field and measures slow field drifts.

[3] This is given by $\sim 0.2\lambda_\mathrm{K}/D$, with $\lambda_\mathrm{K} = 2.2$ μm and $D = 8$ m (Lacour et al. 2014).

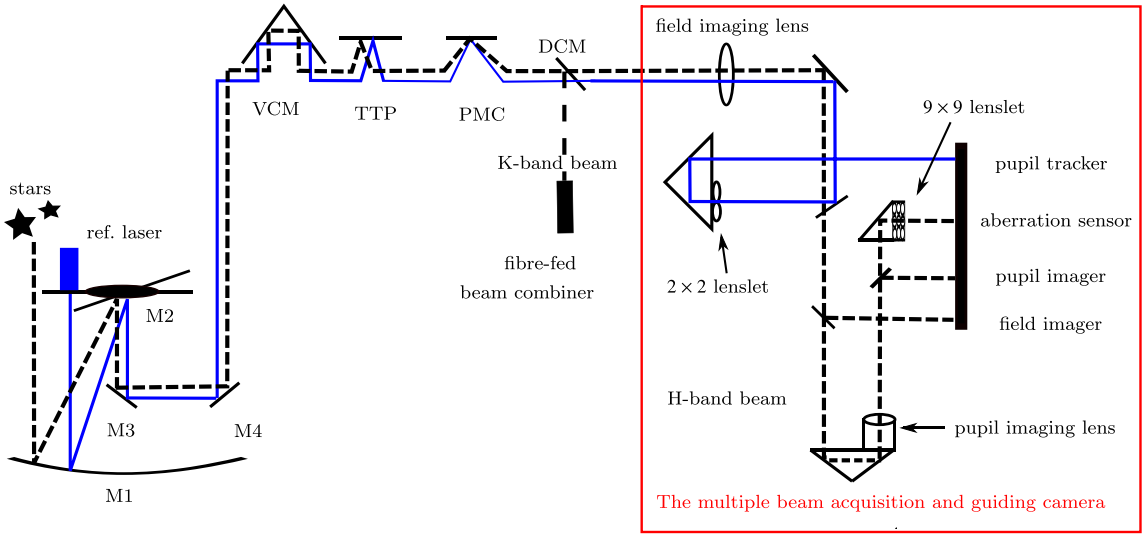

Figure 3. Multiple-beam acquisition and guiding camera conceptual scheme. For simplicity, only one telescope beam case is presented. Only the *H* band (dashed line) and 1.2 μm wavelength (emitted from the reference laser beacon, solid blue line) are used for beam analysis. The *K* band (wide-spaced dashed line) is used for interferometric observations. A dichroic mirror (DCM) splits the incoming telescope beam and sends (a) the reflected light into the fibre-fed beam combiner and (b) the transmitted light *H* band and 1.2 μm wavelength beams into the multiple-beam acquisition and guiding camera (red box). The camera optical functions include (a) pupil tracker, (b) aberration sensor, (c) pupil imager and (d) field imager. The optical functions are used to stabilize the incoming beam and to inject the *K*-band beam into the fibre-fed beam combiner using a variable-curvature mirror (VCM), tip-tilt and piston mirror (TTP) and pupil motion controller (PMC) actuators.

Table 1. UT beam guiding requirements for a $m_H = 13$ mag star (Lacour et al. 2014).

Parameter	Value (rms)
Lateral pupil guiding	≤40 mm
Longitudinal pupil guiding	≤10 km
Field guiding	≤10 mas
Wavefront accuracy	≤80 nm

The multiple-beam acquisition and guiding camera images are used to stabilize the telescope beams using tip-tilt and piston systems, pupil motion controllers (Pfuhl et al. 2014) and variable-curvature mirrors (Ferrari et al. 2003). The tip-tilt and piston systems are actuated mirror controllers placed in the pupil plane of the optical train where incoming beams are propagated. These are used to correct the field drifts. The pupil motion controllers are the pupil lateral shift mirrors located in a field plane of the optical train. They are used to correct the lateral pupil offsets. The variable-curvature mirrors are focus/defocus mirrors placed at the image plane in the VLTI delay lines (Derie 2000). These are used to adjust the position of a pupil longitudinally (pupil focus correction).

The multiple-beam acquisition and guiding camera was defined as a trade-off between the beam guiding requirements (Table 1) for the key Galactic Centre astrometry programme of GRAVITY and the technical constraints (Amorim et al. 2012). The camera is designed to work in *H*-band wavelengths (1.45–1.85 μm) for the following reasons: (a) the Galactic Centre is situated behind ∼ 30 mag of visible extinction (Genzel et al. 2010) and is brighter in the near-infrared, (b) the VLTI throughput is optimized in the infrared as most of the visible light is fed into the visible wavefront sensors at the transmitted Coudé focus (Arsenault et al. 2003) and (c) the *H* band is as close as possible to the science wavelengths (*K* band). To increase stability and to reduce the thermally emitted background, the camera operates at cryogenic temperatures (the detector at 80 K, the beam analyser at ∼110 K and the external folding optics at 240 K). The core optical functions of the camera are manufactured with a single optical material (fused silica, which has a coefficient of thermal expansion of $\sim 10^{-6\circ}C^{-1}$) to minimize stresses when it is cooled down to the cryogenic temperature. The optical functions are imaged on a 2048 × 2048 pix Hawaii-2RG detector (Finger et al. 2008; Mehrgan et al. 2016). The detector is operated in correlated double sampling readout mode with a frame rate of 0.7 s and a readout noise of 13 e^- pix^{-1} rms error. The optical functions of the beam analyser are detailed in the following sections.

2.2 Pupil tracker

The VLTI pupils are re-imaged via delay lines in the GRAVITY beam-combiner instrument. There are several optical pupils, including the delay lines, between the telescope pupil and the GRAVITY fibre-fed beam combiner. The pupils move laterally and longitudinally, due to optical train vibration, while tracking the object of interest. The GRAVITY beam combiner obtains the effective pupil, i.e. the barycentric mean of all these randomly positioned pupil apertures in the whole optical train from the telescope to the beam combiner. The effective pupil is different from the telescope pupil. The typical maximum lateral pupil error is around ∼5 per cent of the pupil (∼0.4 m for an 8 m pupil), much larger than the 40 mm required to achieve 10 μas astrometry (Table 1).

While equalizing the optical paths of the telescopes with the delay lines, the longitudinal pupil position (or pupil defocus) has to be adjusted continually using the delay-line variable-curvature mirrors to preserve the field of the VLTI (2 × 2 arcsec, Ferrari et al. 2003). The variable-curvature mirror corrects the longitudinal pupil positions (pupil defocus) by adjusting its curvature based on a calibration pointing model. Limitations in the pointing model introduce residual longitudinal pupil drifts. The typical maximum longitudinal pupil error is around 30 km at the UT. However, the requirement for 10 μas astrometry is 10 km (Table 1). The pupil

Table 2. Pupil tracker specifications for the UTs.

Parameter	Value
Wavelength	1.2 μm
2 × 2 lenslet	on 2.03 × 2.03 mm
Focal length (f_{PT})	14 mm
Reference beacons separation	1.6 m
Field of view	11.2 m
Pixel scale	59.86 mm pix^{-1}
Detector pixel size (d_p)	18 μm
Field stop	2 × 2 arcsec

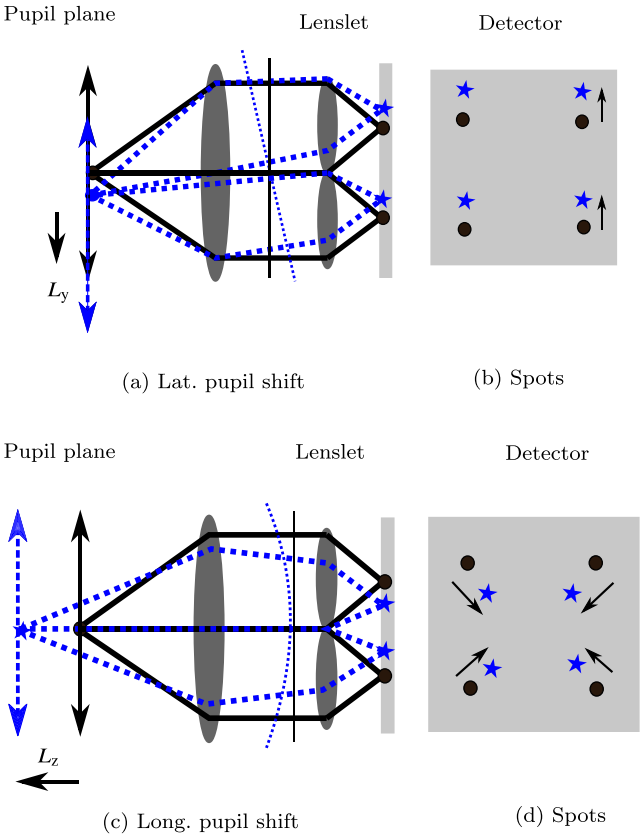

Figure 4. Pupil tracker working principle. The reference telescope pupil and corresponding laser beacon spots are represented by solid black lines and filled circles, respectively. The shifted pupil and corresponding telescope pupil reference laser beacon spots are represented by dashed blue lines and star symbols, respectively. A typical laterally shifted pupil is presented in (a) and (b). A typical longitudinally shifted pupil is presented in (c) and (d).

tracker was designed to measure these pupil shifts (Pfuhl et al. 2012; Amorim et al. 2012).

To detect pupil motion, the telescope pupil is imaged by a 2 × 2 lenslet. Telescope pupil reference laser beacons (1.2 μm) are used. For each telescope, four beacons are mounted on four symmetric spider arms. The barycentre of these four laser beacon positions gives the centre of the pupil. These telescope pupil reference laser beacons are separated by 1.6 m and 0.4 m diagonally on the UTs and ATs, respectively (Table 2).

Fig. 4(a) and (b) illustrate a laterally shifted pupil, i.e. the 2 × 2 lenslet formed spots are laterally shifted from the reference telescope pupil formed spots. Fig. 4(c) and (d) illustrate a longitudinally shifted pupil, i.e. the lenslet formed spots have either converged ($L_z < 0$) or diverged ($L_z > 0$) with respect to the reference spots depending on the direction of the longitudinal displacement.

Table 3. Pupil imager specifications for the UTs.

Parameter	Value
Wavelength	*H* band (1.45–1.85 μm)
Field of view	11.2 m
Pixel scale	54 mm pix^{-1}
Flux for $m_H = 13$ mag	1.8 × 10^4 e$^-$ s^{-1} image^{-1}
Field stop	2 × 2 arcsec

Table 4. Field imager specifications for the UTs.

Parameter	Value
Wavelength	*H* band (1.45–1.85 μm)
Field of view	4 × 4 arcsec
Pixel scale	17.78 mas pix^{-1}
Flux for $m_H = 13$ mag star	4.8 × 10^4 e$^-$ s^{-1}

2.3 Pupil imager

The pupil imager is designed to verify the quality of the pupil image visually (e.g. to identify pupil vignetting or pupil shifts). It is used to align GRAVITY with the VLTI during commissioning and installation and to monitor the telescope pupil visually during observations. It images the telescope pupils using telecentric lenses. Its specifications are presented in Table 3.

2.4 Field imager

The UTs are equipped with adaptive optics based on near-infrared wavefront sensors (CIAO, Scheithauer et al. 2016). The ATs, currently, are equipped only with tip-tilt sensors and they will have adaptive optics modules in the near future (NAOMI, Gonté et al. 2016). In both cases, GRAVITY experiences slow field drifts greater than 10 mas due to its correction residuals and the VLTI tunnel seeing effects. The field imager aims to track this slow field motion. Its specifications are presented in Table 4. The slow field tracking (with a frequency of 1 Hz) is to be complemented by a fast tip-tilt monitoring system. This system works by injecting the visible tip-tilt laser beacon beams before the VLTI tunnel and by imaging them inside GRAVITY, using position sensitive diodes (Pfuhl et al. 2014). It will measure the field motion between the telescopes and GRAVITY.

In GRAVITY, single-mode fibres feed light into the integrated optics (Jocou et al. 2014; GRAVITY Collaboration et al. 2017a), which combines the beams. Light injection into these fibres is stabilized using the field drifts measured by the field imager (Fig. 5). The accurate position of a star $O(x, y)$ is detected by the field imager using the *H*-band beam. Using this position, the single-mode fibre is aligned to the parabola focus with the fibre positioner (Pfuhl et al. 2014). Also using this position, the starlight injection into the single-mode fibre is stabilized using the tip-tilt mirror located in front of the incoming beam.

2.5 Aberration sensor

The aberration sensor is designed to detect the quasi-static residuals of the UT adaptive optics system (Scheithauer et al. 2016). For the ATs, it measures the telescope static aberrations as the ATs are

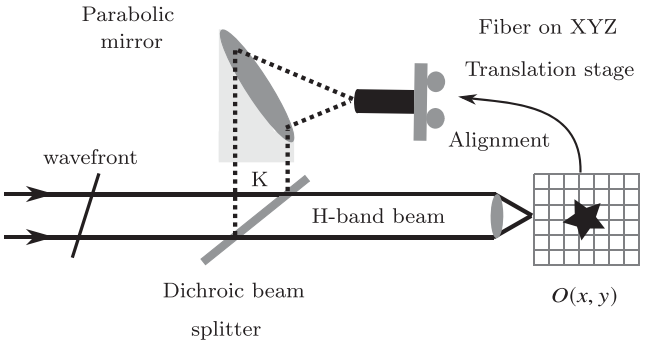

Figure 5. Starlight injection into a single-mode fibre.

Table 5. Aberration sensor specifications for the UTs.

Parameter	Value
Wavelength	*H* band (1.45–1.85 μm)
Lenslet	9 × 9
Field of view per sub-aperture	4 arcsec
Pixel scale	250 mas pix^{-1}
Sub-aperture size	16 × 16 pix^2
Maximum Zernike order measured	28
Sub-aperture flux for an $m_H = 13$ mag star	760 e$^-$ s^{-1}
Field stop	2 × 2 arcsec

not equipped with adaptive optics yet. The measured quasi-static aberrations are used, occasionally, to focus the ATs or to correct the non-common path aberrations between the UT adaptive optics system and GRAVITY. It consists of four Shack–Hartmann sensors, each with 9 × 9 sub-apertures. Its specifications are presented in Table 5.

The pixel-scale magnification in the field between the UTs and the ATs is $8/1.8 = 4.44$, i.e. the field imager scale of 17.78 mas pix^{-1} at the UTs becomes 79 mas for the ATs. The pixel-scale demagnification between the UTs and ATs for the lateral pupil and the longitudinal pupil is $1.8/8 = 1/4.44$ and $(1.8/8)^2 = 1/4.44^2$, respectively.

3 EXTRACTING BEAM GUIDING PARAMETERS

3.1 Image acquisition and analysis software

Dedicated real-time software extracts the beam stabilization parameters from the detector images. The software is implemented within the ESO control software framework. It is written in C and C++ using mainly the ESO standard Common Library for Image Processing (CLIP, Ballester et al. 2008) and Common Pipeline Library (CPL, McKay et al. 2004) and installed in the VLT common software. It works on an instrument workstation running under the Linux operating system and analyses an image in three steps. First, every 0.7 s it integrates the multiple-beam acquisition and guiding camera detector image and stores it in the shared memory of the instrument workstation. Secondly, it copies the detector image from the instrument shared memory and by analysing the input detector image, it evaluates beam tip-tilts, pupil shifts and beam aberrations. These parameters are written to the instrument data base and used for beam stabilization in a closed loop. The multiple-beam acquisition and guiding are carried out in real time on the instrument in parallel with the observations for all four telescopes.

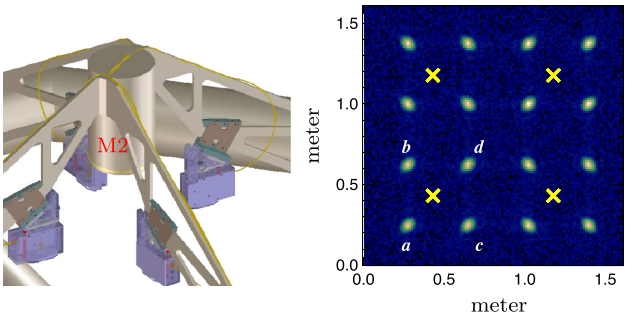

Figure 6. Left: External pupil reference beacons (blue boxes) installed on the telescope secondary mirror M2 spiders. These telescope pupil reference beacons are fed by a common laser diode via multi-mode fibres. Right: A numerically simulated pupil tracker image. The spots *a*, *b*, *c* and *d* are the pupil reference beacons for a sub-aperture. The crosses (×) in the middle are the centres of the lenslet sub-apertures.

3.2 Pupil tracking

The lateral and longitudinal shifts of the telescope pupils are translated as tip-tilt and defocus aberrations when imaged on the 2 × 2 lenslet. The pupil shifts are evaluated by analysing the pupil tracker image in three steps. First, the reference 2 × 2 sub-aperture spots are generated by illuminating an internal reference laser source, which is implemented by the calibration unit (Blind et al. 2014). Next, each sub-aperture j position ($R_j^{x,y}$) is computed by applying Gaussian fits. Secondly, the telescope pupil reference laser beacons spots in the detector image (Fig. 6) are identified using a flux threshold (∼5σ above background) and their full width at half maximum (FWHM) thresholds. Next, their positions are computed. From the spot positions, the centre of each sub-aperture ($C_j^{x,y}$) is determined by taking the average of the telescope reference laser beacon positions. Finally, the spot shifts ($S_j^{x,y}$) are computed by comparing them with the internal reference sub-aperture positions ($R_j^{x,y}$):

$$S_j^{x,y} = C_j^{x,y} - R_j^{x,y}.$$

The telescope lateral pupil shifts are evaluated by taking the average of these spot shifts along the *X* and *Y* directions:

$$L_{x,y} = \frac{1}{4}\sum_{j=1}^{4} S_j^{x,y}. \quad (2)$$

The longitudinal pupil shifts are evaluated by computing the amount of convergence or divergence (in radians) of the spot shifts (equation 3 of Salas-Peimbert et al. 2005):

$$L_z = \frac{d_p}{f_{PT}} \frac{(S_2^x + S_3^x) - (S_1^x + S_4^x) + (S_1^y + S_2^y) - (S_4^y + S_3^y)}{8}, \quad (3)$$

where f_{PT} is the focal length of the 2 × 2 lenslet and d_p the detector pixel size (Table 2).

3.3 Pupil imaging

The pupil imager is used to monitor the quality of the telescope pupils visually during the preparation for observations and also while observing. However, it can also be used, in future, for lateral pupil tracking with a bright astrophysical source. A cross-correlation algorithm (Poyneer 2003) allows the pupil shift to be

computed from a shifted pupil image by correlating it with the reference pupil image.[4]

3.4 Object tracking with the field imager

The field imager measures these field drifts by tracking the brightest object in the user-specified region (window) of interest. Windowing is important in crowded regions such as the Galactic Centre. The position of the brightest object is computed in two steps. First, stars in the field are scanned using a 5σ flux threshold above background and a predetermined FWHM. Next, the detected stars are sorted into decreasing flux order. Secondly, an accurate position of the brightest object $O(x, y)$ is computed with a Gaussian fit in a window size of $8 \times 8\,\mathrm{pix}^2$ centred on the object. To track binaries where both stars are of comparable magnitude, the position of the second brightest object within the window is also measured and the tracking reference is chosen by the instrument operator.

The atmospheric differential refraction effects are of relevance because the H-band photo-centre is used to estimate the fibre coordinates used to inject the K-band beam into the fibre. The shift (ΔR) caused by the atmospheric differential refraction (e.g. Roe 2002) is

$$\Delta R \simeq 206\,265 \left(\frac{n_{\lambda_\mathrm{K}}^2 - 1}{2n_{\lambda_\mathrm{K}}^2} - \frac{n_{\lambda_\mathrm{FI}}^2 - 1}{2n_{\lambda_\mathrm{FI}}^2} \right) \tan\zeta \ [\mathrm{arcsec}], \quad (4)$$

with λ_FI and λ_K the field imager (H band) and the fibre (K band) accepting wavelengths, n_{λ_FI} and n_{λ_K} the corresponding refractive indices, and ζ is the object zenith distance. The refractive index for a given wavelength as a function of the observing conditions (temperature, pressure and humidity) is computed using equation (1) in Roe (2002).

Since the effective wavelength of the field imager λ_FI changes with the colour of the object, its value is modelled (Stone 2002) as a function of the $H - K$ colour by considering the atmospheric transmission and the instrument transmission.[5]

The correction for the atmospheric differential refraction object offset (ΔR) is applied in real time given the $H - K$ object colour inserted by the observer in the observing block.

3.5 Beam wavefront sensing with the aberration sensor

The aberrated wavefront is reconstructed by comparing the reference Shack–Hartmann spot locations with the aberrated spot locations. The reference spots were obtained as part of the calibration procedure using a collimated beam. During the observations, the spots of incoming telescope beams are acquired. The centroids of these spots are computed by applying Gaussian fits. When an extended scene is observed, the centroids are computed using a cross-correlation algorithm (Poyneer 2003). The slopes of the spot shifts are computed by taking the differences between the target and the reference spot positions. These slopes are normalized by the focal length of the lenslet. Using these slopes, higher-order aberrations of the input beams are evaluated in terms of up to 28 of Noll's Zernike coefficients (Dai 1996).

[4] The reference pupil image is the pupil image when one wants to lock the pupil during observations. It can be a long exposure image of a telescope pupil.

[5] The product of the transmission for all filters, the reflection of the mirrors and the efficiency of the detector as a function of wavelength.

Table 6. End-to-end simulation of the accuracy of the guiding parameters and comparison with the requirements.

Parameter	Requirement (rms)	Simulation (rms)
Lateral pupil guiding	≤40 mm	≤4 mm
Longitudinal pupil guiding	≤10 km	≤200 m
Field guiding	≤10 mas	≤2 mas
Wavefront measurement	≤80 nm	≤70 nm

3.6 End-to-end simulations

Meticulous numerical modelling of the multiple-beam acquisition and guiding camera was carried out to verify the beam analysis methods. These simulations are implemented in the YORICK[6] programming language, which provides easy interpretation, debugging and plotting. The LIGHTPIPES (Vdovin, van Brug & van Goor 1997) ANSI C library was ported to YORICK and the adaptive optics YAO (Rigaut & Van Dam 2013) library was used.

The detector images of the multiple-beam acquisition and guiding camera were generated using the optomechanical model parameters (with ZEMAX, Amorim et al. 2012) and by applying the field motions, pupil motions (lateral and longitudinal) and higher-order wavefront aberrations experimentally measured by the VLTI laboratory. Finally, the input beam aberrations were reconstructed. The performance of the multiple-beam acquisition and guiding camera was characterized in terms of its accuracy under adverse imaging conditions and its sensitivity to faint stars. Table 6 presents the numerical analysis of the accuracy of the multiple-beam acquisition and guiding camera.

4 LABORATORY CHARACTERIZATION

The multiple-beam acquisition and guiding camera was characterized using the GRAVITY calibration unit in the Max Planck Institute for extraterrestrial Physics (MPE) laboratory (Blind et al. 2014). The calibration unit simulates an artificial launch telescope with a parabolic mirror and two artificial stars with 95 per cent Strehl ratio by illuminating two single-mode fibres. The four telescope pupil reference laser beacon beams are generated by four multi-mode fibres inserted in a pupil plane. Fig. 7 presents the imaging modes of the camera, for one telescope, when illuminated by the calibration unit.

The field of view of the pupil tracker, pupil imager and aberration sensor are estimated by scanning (applying tilts) a target star over their field of view. During the scanning, the flux and position of the target are recorded in each window. Fig. 8 presents the flux in the pupil tracker, pupil imager and aberration sensor windows as a function of target star position. The field stop of each optical function is apparent in the width of the curves in Fig. 8, being ∼2 arcsec. The field stops as built matched the design values (Tables 2, 3 and 5).

4.1 Pupil tracking performance

The pupil tracker pixel scale is measured by equating the separation of telescope pupil reference laser beacons observed on the detector to the separation of those beacons installed on the telescope of the calibration unit. The measured value is within 5 per cent of the design value (Table 2).

[6] http://yorick.sourceforge.net/

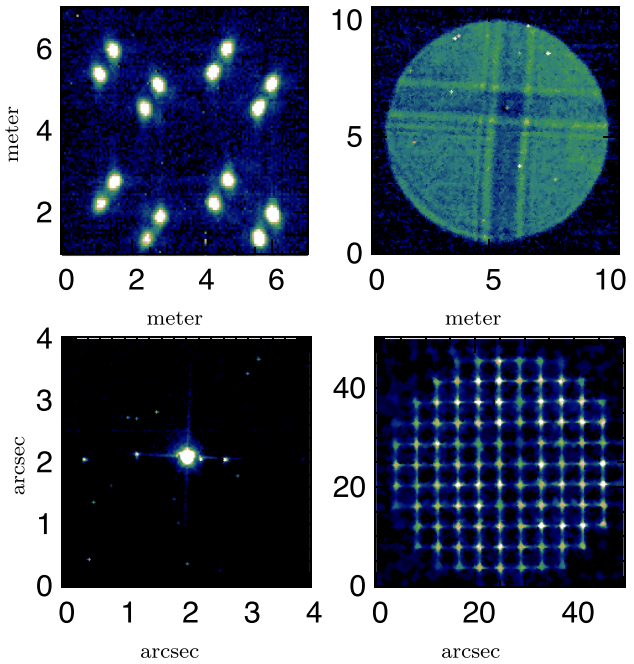

Figure 7. Optical imaging modes of the camera obtained using the beams generated by the calibration unit. Images are scaled to the UT magnification. Top left: Pupil tracker. Top right: Pupil imager. Bottom left: Field imager. Bottom right: Aberration sensor imager. The complex structure in the pupil image is laboratory specific (Blind et al. 2014).

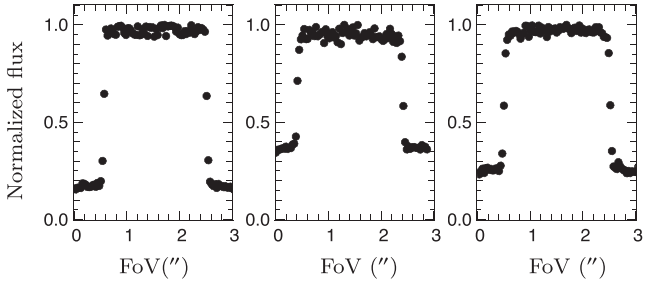

Figure 8. Target normalized flux as a function of position for the pupil tracker, pupil imager and aberration sensor windows (from left to right).

The performance of the lateral pupil tracking is characterized in the laboratory by manipulating the pupil lateral correcting actuators. This experiment is carried out in two steps. First, known lateral pupil shifts are applied to the incoming beams by actuating the pupil lateral correcting actuators. Secondly, the input pupil shifts are estimated from the pupil tracker images as explained in Section 3.2. Fig. 9 shows that measurements of the lateral pupil position agree with the end-to-end simulations and are 10× better than the requirement. The longitudinal pupil tracking could not be characterized at the MPE laboratory because of the unavailability of longitudinal pupil actuators inside the GRAVITY instrument. This was tested at the VLTI laboratory using the variable-curvature mirrors available in the delay lines (Section 5).

4.2 Field tracking performance

To characterize the performance of the field tracker, known tip-tilt values $\alpha_{\rm in}$ were applied to the incoming beams and measured back as $\alpha_{\rm out}$ using the field tracker, as explained in Section 3.4. The tip-tilts to the incoming beams are applied using the tip-tilt actuators. The

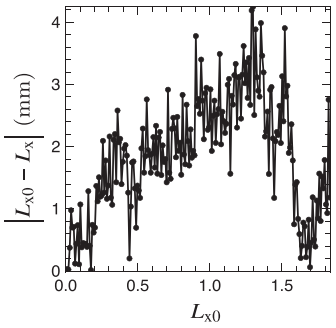

Figure 9. Absolute error in the lateral pupil position measurement (UT beam) as a function of input lateral pupil shift in the laboratory. The error bars are rms errors.

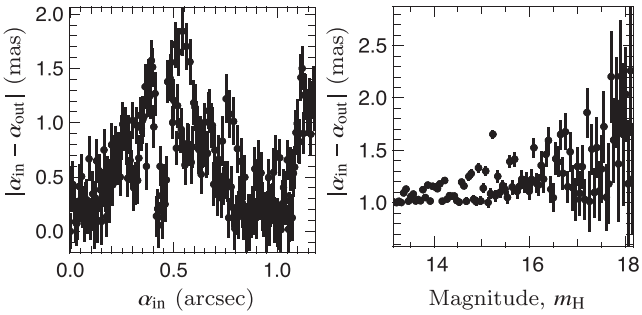

Figure 10. Performance of the field tracker in the laboratory for the UT set-up. Left: The absolute error as a function of the object's true position. The observed shape is due to the mechanical instability of the tip-tilt correcting system. Right: The absolute error of object tracking as a function of star magnitude $m_{\rm H}$. The error bars are rms errors.

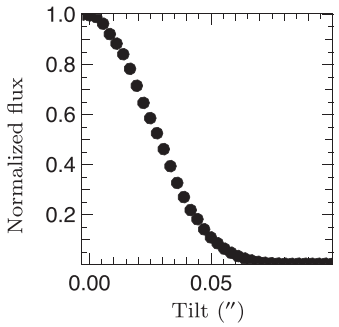

Figure 11. Fibre injection performance in the laboratory.

left-hand panel of Fig. 10 presents the absolute error of the object position as a function of the known input tilt. The error is less than 2 mas. These measurements are done under high signal-to-noise conditions, i.e. with a negligible contribution from readout noise centroid error. The right-hand panel of Fig. 10 presents the absolute rms error as a function of the magnitude of the star. An absolute rms error of 1 mas is observed for the equivalent of a $m_{\rm H} = 13$ mag star.

4.2.1 Injection performance

Fig. 11 shows how the injection of starlight into the fibre drops with unwanted tilts. From the figure, it can also be seen that the size of the fibre core is around 60 mas. Using the field stabilization enabled by the field tracker, the coupling efficiency of the fibre is maintained at around 75 per cent.

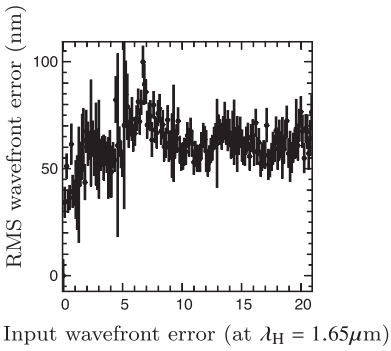

Figure 12. The rms wavefront error as a function of the input wavefront applied at the laboratory (UT beam). The error bars are rms errors.

4.2.2 Atmospheric differential refraction

The importance of the atmospheric differential refraction offset ΔR (equation 4) can be computed using the effective wavelengths and the zenith angle $\zeta = 30°$. It is ~ 22 mas (which corresponds to a shift of $\sim$1.23 pix) and corresponds to a $\sim$20 per cent loss of injection of light into the fibre.

4.3 Beam aberration sensing and performance

The performance test to estimate the aberration sensor wavefront was carried out in two steps. First, the focal lengths of the Shack–Hartmann lenslet were calibrated by applying a series of tilts to the incoming plane wavefront (Kumar, Narayanamurthy & Kumar 2013). Secondly, to measure the accuracy of the aberration sensor, known tip-tilt and defocus wavefront aberrations were applied to the incoming beams, which were measured back using the aberration sensor function as explained in Section 3.5. Fig. 12 presents the rms wavefront error observed as a function of the input wavefront (tip, tilt and defocus rms errors). It can be seen that the wavefront accuracy is $\sim\lambda/20$ at the UT scale. In this experiment, a sub-aperture flux equivalent to a $m_H = 11$ mag star ($\sim$2500 ADU s^{-1}) is used. ADU is abbreviation to Analog to Digital Units.

5 ON-SKY CHARACTERIZATION

5.1 Image quality characterization

Based on verification tests at MPE, the GRAVITY instrument passed Preliminary Acceptance Europe (PAE) in 2015 May. The instrument was then deployed at the Paranal Observatory, Chile, and received its first light in 2015 November. Fig. 13 presents the multiple-beam acquisition and guiding camera detector image acquired on-sky with the UTs. Table 7 presents the Strehl ratio and the star FWHM at the camera when it was illuminated using the calibration unit. Also, the pixel scale that was measured at the laboratory and at the Paranal Observatory on-sky are presented.

The sky field of view of the camera is larger than the nominal VLTI field of view (2 × 2 arcsec). This is confirmed by (long exposure) imaging of the sky with the field imager and by moving the VLTI star separator tip-tilt mirrors (FSM, Delplancke et al. 2004) in several steps. Fig. 14 presents the VLTI field of view, which is around 3.6 × 3.6 arcsec at the UTs. This is less than the design value of 4 × 4 arcsec (Table 4).

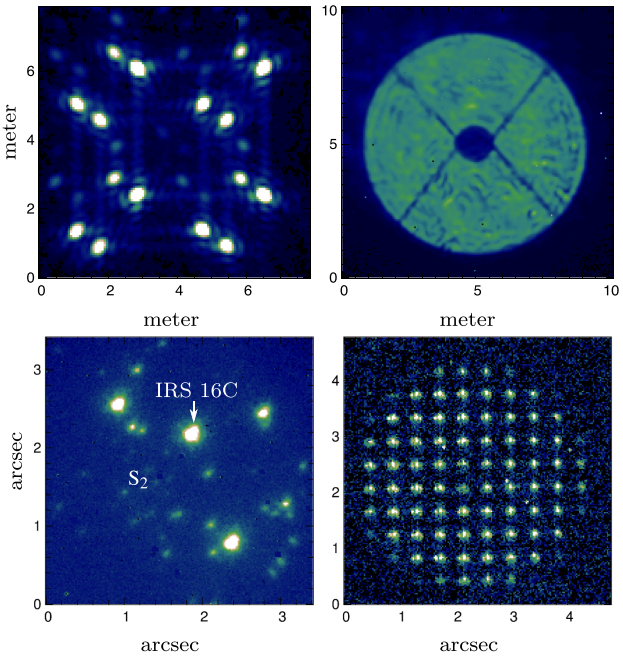

Figure 13. Imaging modes of the camera observed on-sky with the UTs. Top left: The pupil tracker. Top right: The pupil imager. The low-intensity cross stripes visible in the pupil imager are the holding spiders of the secondary mirror. Bottom left: The field tracker. Bottom right: The aberration sensor. The astrophysical target is the Galactic Centre. The aberration sensor image is rotated counterclockwise to the field image due to a mirror reflection (π phase).

Table 7. Field imager Strehl ratio, FWHM and pixel scales as built (at the UT scale).

Telescope arm	StrehlFWHM ratio at lab	Pixel scale at lab (pix)	Pixel scale at lab (mas pix^{-1})	on-sky (mas pix^{-1})
T1	0.90	2.65	18.23	17.77
T2	0.85	3.12	18.51	18.00
T3	0.70	3.18	18.20	17.64
T4	0.63	3.51	18.76	19.53

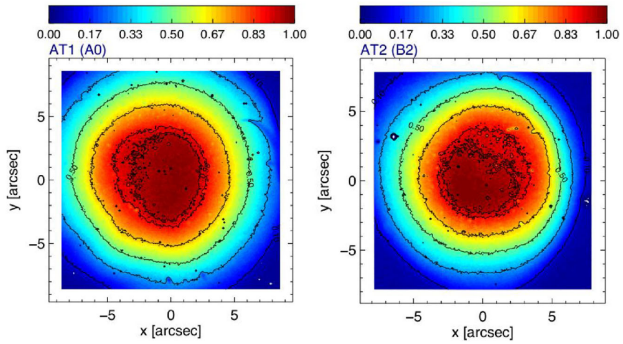

Figure 14. Representative fields of view of the field imager measured at two AT stations. The colour represents the normalized flux.

5.2 Characterization of the pupil tracker

The performance of the longitudinal pupil tracking was characterized at the VLTI laboratory by injecting artificial light source beams into the GRAVITY instrument via the delay lines, using the

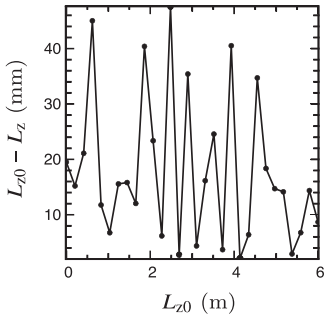

Figure 15. Longitudinal pupil shift residuals as a function of input longitudinal pupil shift (L_{z0}) at the VLTI for an UT beam.

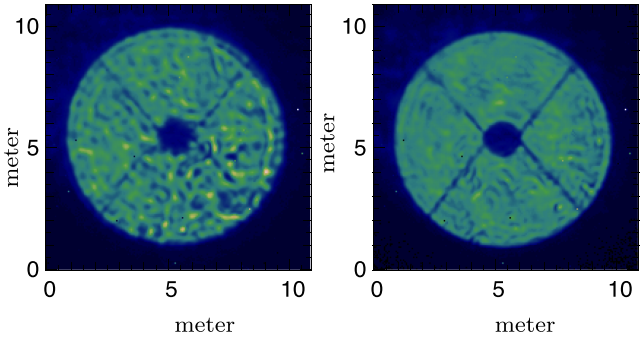

Figure 16. UT pupil images obtained before (left) and after (right) closing the pupil guiding loop.

ARAL facility (Morel et al. 2004). The longitudinal pupil shifts were simulated by manipulating the delay-line variable-curvature positions. Known longitudinal pupil shifts (L_{z0}) were applied to the beam by moving the variable-curvature mirror and the input shifts were measured (L_z) using the pupil tracker function as explained in Section 3.2. The longitudinal pupil accuracy (Fig. 15) is better than 400 m (i.e. 10^4 magnification between the 8 m telescope and 80 mm beam inside the lab). Fig. 16 presents the UT pupil before and after closing the pupil guiding loop. After closing the pupil guiding loop, an improvement in the pupil focus can be seen.

5.2.1 Bright target performance

The pupil tracker experiences high background levels from bright astrophysical targets observed in the *J* and *H* bands (a) due to the closeness of the operating wavelengths of the pupil tracker (1.2 μm) and the field imager and (b) because no adequate filter is available for the pupil tracker. The best operation of pupil guiding is possible when (a) the flux of the telescope pupil reference laser beacons is high and (b) imaging a lower magnitude or red astrophysical target (with low flux at 1.2 μm). The background problem is solved to a certain extent on two fronts: (a) using the neutral density attenuation filters[7] and (b) using the BLINK mode. This mode removes the background by taking two frames with the laser beacons on and off. The exposure with the beacons on is subtracted from the exposure with the beacons off. This effectively removes the background caused by the astrophysical target. With this mode, the performance of pupil guiding is additionally improved by 2 mag. The performance of pupil guiding as a function of target magnitude is presented in

[7] To avoid saturating the camera detector for bright astrophysical targets, GRAVITY is equipped with *H*-band neutral density attenuation filters (10 and 5 mag) in front of the camera.

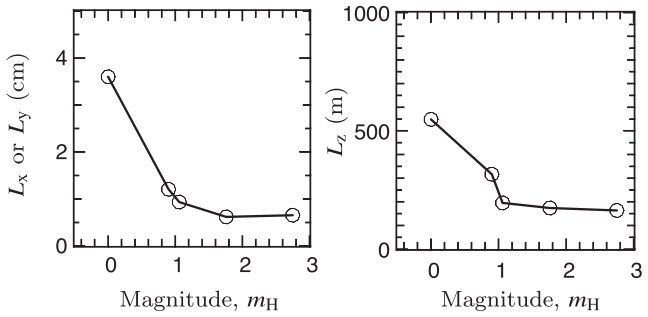

Figure 17. Pupil tracker performance (scaled to the UTs) as a function of the magnitude of several target stars. Left: Lateral pupil residuals along the *X* or *Y* directions. Right: Longitudinal pupil residuals.

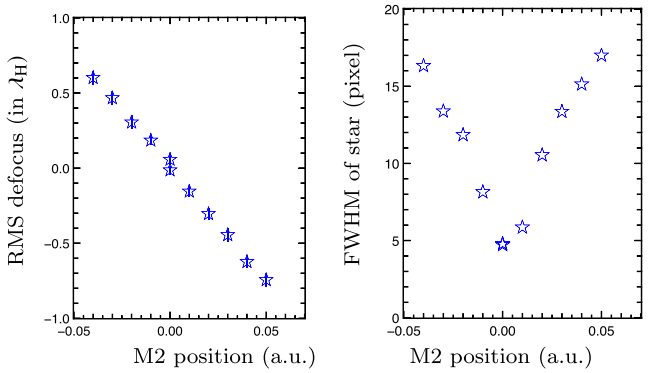

Figure 18. Focusing calibration of the ATs with the aberration sensor. Left: Zernike defocus coefficient rms versus M2 focus position (in arbitrary units, a.u.). Right: The corresponding FWHM of a star observed in the field imager.

Fig. 17. The pupil tracker performance degrades significantly for targets brighter than $m_H = 1$ mag.

5.3 The pupil imager

The pupil imager is, currently, used visually to monitor the quality of the telescope pupils during the preparation for observations and also while observing. However, it can also be used for lateral pupil tracking with a bright astrophysical source to complement the problem of the pupil tracker (Section 3.3).

5.4 Calibration of the aberration sensor focus

The aberration sensor is used to correct the focus of the ATs. Fig. 18 shows the measured aberration sensor focus as a function of the secondary mirror (M2) position (in arbitrary units). The right-hand panel presents the corresponding star FWHM measured by the field imager.

5.5 The field and pupil guiding residuals

Stabilization of the field and pupil beam are achieved with two types of actuators. The smaller field and pupil offsets during interferometric observations are corrected in the closed loop using the GRAVITY internal actuators for speed and accuracy. Larger field and pupil offsets, which usually occur during the initial alignment of GRAVITY, are corrected using the VLTI-based star separator actuators and delay-line variable-curvature mirror. If when operating in closed loop the offsets are larger than the range of the internal actuators, they are offloaded to the VLTI star separator actuators.

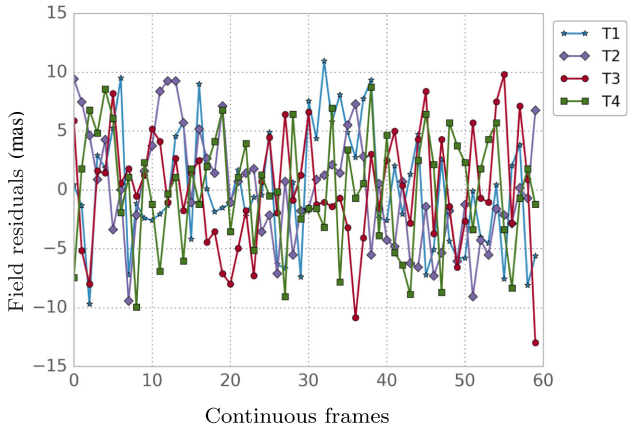

Figure 19. Field guiding residuals for object HD 141742 ($m_H = 6.17$) when observed with the UTs on 2016 September 15. A neutral density filter of 5 mag was used.

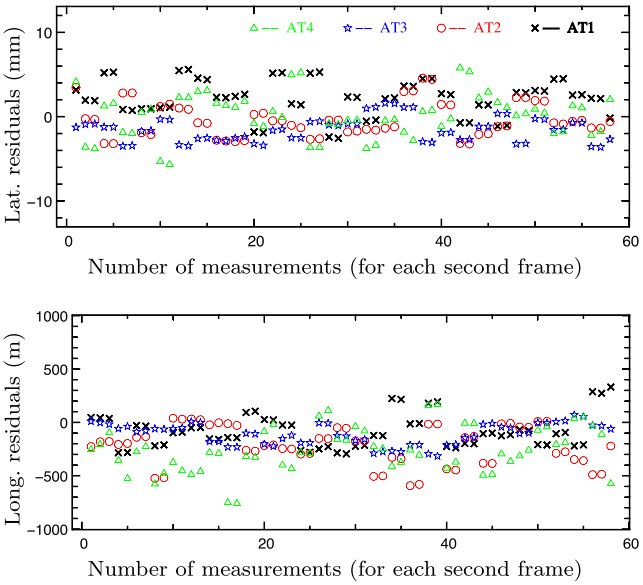

Figure 20. Pupil guiding residuals observed for the ATs for 60 frames on 2016 March 19. The measured pupil shifts are scaled to the UT scale. The astrophysical target has $m_H = 1.74$. The pupil tracker is operated in the BLINK mode during this experiment.

Often, GRAVITY experiences optical misalignments with the VLTI. In the worst case, there are field offsets of ∼60 mas rms and lateral pupil offsets of ∼5 per cent (0.4 m rms) in the UT pupil. With beam guiding enabled by the multiple-beam acquisition and guiding camera, the field, lateral pupil and longitudinal pupil guiding are implemented with standard deviation residuals smaller than ±0.5 pix rms (10 mas rms), ±0.2 pix rms (12 mm rms) and ±400 m rms at the UT, respectively. Figs 19 and 20 present the field and pupil guiding residuals.

5.6 Astrometric residuals study

The total astrometric error produced by the four telescopes (equation 1) adds to

$$\sigma_{4T} = \sqrt{\sum_{i=1}^{4} \sigma_{T,i}^2}. \quad (5)$$

Table 8. Astrometric error at the UT due to field and pupil residuals.

Residual errors	One telescope	Four telescopes
Without beam guiding residuals		
$\Delta\alpha \leq 60$ mas	316.6 μas	≤633.3 μas
$\Delta L_x \leq 0.4$ m	δOPD ≤ 153.5 nm	
$\Delta L_z \leq 30$ km		
Beam guiding requirements		
$\Delta\alpha \leq 10$ mas	4 μas	≤8 μas
$\Delta L_x \leq 40$ mm	δOPD ≤ 1.95 nm	
$\Delta L_z \leq 10$ km		
Laboratory beam guiding residuals		
$\Delta\alpha \leq 2$ mas	–	–
$\Delta L_x \leq 4$ mm		
$\Delta L_z \leq 400$ m		
On-sky beam guiding residuals		
$\Delta\alpha \leq 10$ mas	1.2 μas	≤2.4 μas
$\Delta L_x \leq 12$ mm	δOPD ≤ 0.58 nm	
$\Delta L_z \leq 400$ m		

The astrometric error caused by the field and the pupil motion is around 633.3 μas and 2.4 μas before and after closing the beam guiding loop, respectively, at the UT and for the baseline of 100 m. Table 8 summarizes the guiding requirements and the achieved beam guiding for several conditions. The on-sky residuals are larger than the laboratory characterization (using the beams generated by the calibration unit) because the frame rate of the multiple-beam acquisition and guiding camera (0.7 s) is not quick enough to correct them.

A GRAVITY observation is described in detail in GRAVITY Collaboration et al. (2017a). An animation of starlight tracing through the GRAVITY instrument is available elsewhere.[8]

Operation of GRAVITY with the multiple-beam acquisition and guiding camera started with the ATs in 2016 October and with the UTs in 2017 April. The first light and science verification results from GRAVITY are published in, e.g., GRAVITY Collaboration et al. (2017a,b, 2017c, López-Gonzaga et al. 2017), Le Bouquin et al. (2017) and Kraus et al. (2017). The first verification of the narrow-angle astrometry of GRAVITY was done with an M-dwarf binary, GJ 65. The binary separation was estimated with residuals of 50 μas (GRAVITY Collaboration et al. 2017a). However, the astrometric residual errors can be reduced further by computing the guiding residual errors carefully from the multiple-beam acquisition and guiding camera images off-line in the data reduction pipeline and inputting them into the astrometric calculations. There are also other possible error contributors in the GRAVITY measurements but they are out of the scope of this paper to be described in detail: (a) uncertainty in the calibration of the narrow-angle astrometric baseline and wavelength and (b) dispersion in the single-mode fibres and integrated optics.

6 SUMMARY AND CONCLUSIONS

Accurate beam acquisition and guiding camera methods for phase referencing optical and infrared interferometry are presented. These methods offer advances in near-infrared imaging and optical and infrared long-baseline interferometry: (a) the accurate and active pupil and field guiding necessary for sensitivity and astrometry and (b) the characterization of the quality of the input telescope beams,

[8] http://www.eso.org/public/videos/eso1622b/

the focus correction for the ATs and the possibility of correcting the non-common path aberration errors between the adaptive optics system and GRAVITY.

The performance of the beam acquisition and guiding camera was verified using laboratory-generated telescope beams and on-sky at the VLTI. The characterization results show that it is able to analyse the telescope beams: (a) field tracking in a crowded field with $\lesssim$ 10 mas rms residuals translates to a 75 per cent coupling efficiency of near-infrared starlight into single-mode fibres, (b) lateral pupil tracking with residuals less than 12 mm rms, (c) longitudinal pupil tracking with residuals less than 400 m rms and (d) quasi-static higher-order wavefront aberration measurements with 80 nm rms. The beam parameters measured by the multiple-beam acquisition and guiding camera were used to stabilize the field and pupil and to correct the AT focus. The pupil imager is used to monitor visually the quality of the telescope pupils during the preparation for observations and also while observing. Overall, the performance of the camera meets the requirements of the GRAVITY science programmes, although some work is still needed to push the residual errors down further by implementing the post-processing of the multiple-beam acquisition and guiding camera images in the data reduction pipeline and also by correcting the non-common path aberration errors between the adaptive optics and GRAVITY.

Camera imaging assisted by adaptive optics is an asset for the GRAVITY science observations as it provides *H*-band images of the target using four different telescopes, simultaneously, in parallel to the interferometric observations in the *K* band. Provided that the camera is astrometrically calibrated (e.g. Yelda et al. 2010), field images from the multiple-beam acquisition and guiding camera can be useful in three ways: (a) to extend the wavelength coverage in the *H* band (1.45–1.85 μm), (b) to extend the spatial resolution coverage (with low-resolution images from the field imager and high-resolution images from the interferometric large baselines) and (c) to solve the 2π interferometric phase wrapping ambiguity.[9]

Although the multiple-beam acquisition and guiding camera is a subsystem of GRAVITY, it can be used for other interferometric beam-combiner instruments available at the VLTI (e.g. MATISSE, Lopez et al. 2014) in automated alignment with the VLTI and in closed-loop tip-tilt guiding. Furthermore, the accurate pupil guiding developed here is relevant (a) to high-contrast imaging, which requires extreme adaptive optics enabled by pupil stabilization (e.g. SPHERE, Montagnier et al. 2007), (b) to correct the misregistration of pupils between the wavefront sensor and the deformable mirror when there are moving optics parts in between[10] and (c) to the accurate alignment of the pupil mask to match the telescope pupil to limit the background radiation coming into the spectrograph (e.g. HARMONI, Hernández et al. 2014). The pupil tracker allows both the telescope pupil rotation and the lateral shifts to be estimated accurately.

ACKNOWLEDGEMENTS

We thank the technical, administrative and scientific staff of the participating institutes and the observatory for their extraordinary support during the development, installation and commissioning of GRAVITY. We thank the referee for their constructive and insightful report. NA acknowledges Fundação para a Ciência e a Tecnologia and the International Doctorate Network in Particle Physics, Astrophysics and Cosmology (IDPASC), Portugal for his PhD grant SFRH/BD/52066/2012. The research leading to these results received funding from PTDC/CTE-AST/116561/2010, COMPETE FCOMP-01-0124-FEDER-019965 and UID/FIS/00099/2013. This research was partially funded by the European Commission Seventh Framework Programme, under grant agreements 226604 and 312430 (Optical Infrared Coordination Network for Astronomy – OPTICON). We acknowledge support from the ERC Starting Grant 'ImagePlanetFormDiscs' (Grant Agreement No. 639889).

REFERENCES

Amorim A., Lima J., Anugu N. et al., 2012, Proc. SPIE, 8445, 844534
Arsenault R. et al., 2003, Proc. SPIE, 4839, 174
Ballester P., Biereichel P., Kaufer A., Kiekebusch M., Lorch H., 2008, ASP Conf. Ser. Vol. 394, ADASS XVII. Astron. Soc. Pac., San Francisco, p. 577
Benisty M., Berger J.-P., Jocou L., Labeye P., Malbet F., Perraut K., Kern P., 2009, A&A, 498, 601
Blind N. et al., 2014, Proc. SPIE, 9146, 91461U
Colavita M. M., 2009, New Astron. Rev., 53, 344
Dai G. M., 1996, J. Opt. Soc. A, 13, 1218
Delplancke F., Nijenhuis J., Man H., Andolfato L., Treichel R., Hopman J., Derie F., 2004, Proc. SPIE, 5491, 1528
Derie F., 2000, Proc. SPIE, 4006, 25
Eisenhauer F. et al., 2011, Messenger, 143, 16
Ferrari M. et al., 2003, Proc. SPIE, 4838, 1155
Finger G., Dorn R. J., Eschbaumer S., Hall D. N., Mehrgan L., Meyer M., Stegmeier J., 2008, Proc. SPIE, 7021, 70210
Genzel R., Eisenhauer F., Gillessen S., 2010, Rev. Modern Phys., 82, 3121
Gonté F. Y. J. et al., 2016, Proc. SPIE, 9907, 990720
GRAVITY Collaboration Abuter R. et al., 2017a, A&A, 602, A94
GRAVITY Collaboration Waisberg I. et al., 2017b, ApJ, 844
GRAVITY Collaboration Petrucciet P.-O. et al., 2017c, A&A, 602, L11
Hernández E. et al., 2014, Proc. SPIE, 9151, 91513F
Jocou L. et al., 2014, Proc. SPIE, 9146, 91461J
Kraus S. et al., 2017, ApJ, 835, L5
Kumar M. S., Narayanamurthy C. S., Kumar A. S. K., 2013, Opt. Eng., 52, 12
Lacour S. et al., 2014, A&A, 7, A75
Le Bouquin J.-B. et al., 2017, A&A, 601, A34
Lippa M. et al., 2016, Proc. SPIE, 9907, 990722
Lopez B. et al., 2014, Messenger, 157, 5
López-Gonzaga N., Asmus D., Bauer F. E., Tristram K. R. W., Burtscher L., Marinucci A., Matt G., Harrison F. A., 2017, A&A, 602, A78
McKay D. J. et al., 2004, Proc. SPIE, 5493, 444
Mehrgan L. H., Finger. G., Eisenhauer F., Panduro J., 2016, Proc. SPIE, 9907, 99072F
Montagnier G. et al., 2007, Opt. Express, 15, 23
Morel S. et al., 2004, Proc. SPIE, 5491, 1079
Pfuhl O. et al., 2012, Proc. SPIE, 8445, 84451U
Pfuhl O. et al., 2014, Proc. SPIE, 9146, 914623
Poyneer L. A., 2003, Appl. Opt., 42, 5807
Rigaut F., Van Dam M., 2013, Proc. AO4ELT 3, 2013
Roe H. G., 2002, PASP, 114, 450
Salas-Peimbert D. P., Malacara-Doblado D., Durán-Ramírez V. M., Trujillo-Schiaffino G., Malacara-Hernández D., 2005, Appl. Opt., 44, 4228
Scheithauer S. et al., 2016, Proc. SPIE, 99092L
Stone R., 2002, PASP, 114, 1070
Vdovin G., van Brug H., van Goor F., 1997, Proc. SPIE, 3190, 19
Woillez J., Lacour S., 2013, ApJ, 764, 109
Yelda S., Lu J. R., Ghez A. M., Clarkson W., Anderson J., Do T., Matthews K., 2010, ApJ, 725, 331

[9] If the two stars are separated by more than λ/B, they suffer from the 2π phase wrapping ambiguity.

[10] For example, when the deformable mirror is at the telescope or the Coudé focus and the wavefront sensor is inside the beam-combiner laboratory.

This paper has been typeset from a TEX/LATEX file prepared by the author.